

Effect of NaOH content on hydration, mineralogy, porosity and strength in alkali/sulfate-activated binders from ground granulated blast furnace slag and phosphogypsum

Peer-reviewed author version

GIJBELS, Katrijn; Pontikes, Yiannis; SAMYN, Pieter; SCHREURS, Sonja & SCHROEYERS, Wouter (2020) Effect of NaOH content on hydration, mineralogy, porosity and strength in alkali/sulfate-activated binders from ground granulated blast furnace slag and phosphogypsum. In: Cement and Concrete Research, 132 (Art N° 106054).

DOI: 10.1016/j.cemconres.2020.106054

Handle: <http://hdl.handle.net/1942/30999>

**EFFECT OF NaOH CONTENT ON HYDRATION, MINERALOGY,
POROSITY AND STRENGTH IN ALKALI/SULFATE-ACTIVATED
BINDERS FROM GROUND GRANULATED BLAST FURNACE SLAG
AND PHOSPHOGYPSUM**

Katrijn GIJBELS^{a*}, Yiannis PONTIKES^b, Pieter SAMYN^c, Sonja SCHREURS^a, Wouter
SCHROEYERS^a

^a Hasselt University, CMK, Nuclear Technological Centre, Agoralaan, Gebouw H, 3590
Diepenbeek, Belgium

^b KU Leuven, Department of Materials Engineering, Kasteelpark Arenberg 44, 3001 Leuven,
Belgium

^c Hasselt University, IMO-IMOMEC, Applied and Analytical Chemistry, Agoralaan, Gebouw
D, 3590 Diepenbeek, Belgium

* Corresponding author: Katrijn GIJBELS

katrijn.gijbels@uhasselt.be, yiannis.pontikes@kuleuven.be, pieter.samyn@uhasselt.be,
sonja.schreurs@uhasselt.be, wouter.schroeyers@uhasselt.be

Declarations of interest: none

Abstract

This study investigates the effect of NaOH content on alkali/sulfate-activated binders from 90 wt.% ground granulated blast furnace slag (GGBFS) and 10 wt.% phosphogypsum (PG). Alkali activators were prepared with a NaOH molarity ranging from 0 M to 4 M. The hydration was monitored using in-situ X-ray diffraction (XRD) and isothermal calorimetry. The hydration product assemblage was investigated using XRD, thermogravimetric analysis (TGA), Fourier-transformed infrared (FTIR) spectroscopy, nitrogen adsorption/desorption and compressive strength tests. A molarity of 0 M NaOH gave rise to the highest porosity and highest strength, although setting occurred only after 7 days. From a molarity of 2 M NaOH and higher, ettringite disappeared and got replaced by a monosulfate phase (i.e., $\text{NaCa}_4\text{Al}_2\text{O}_6(\text{SO}_4)_{1.5} \cdot 15\text{H}_2\text{O}$) and amorphous aluminum-hydroxide. This study shows the potential of using GGBFS and PG for the development of novel by-product based cementitious binders.

Keywords

Ground granulated blast furnace slag, phosphogypsum, supersulfated cement, alkali-activated binder

1. Introduction

Compared to other conventional construction products, such as steel or aluminum, the average CO_2 emission of ordinary Portland cement (OPC) production is relatively low (0.83 tonnes/tonne OPC, 3 tonnes/tonne steel and 15 tonnes/tonne aluminum) [1–3]. Due to the enormous global production volumes, however, it makes a significant contribution to overall global CO_2 emissions [1,2,4], together with the fact it is difficult to recycle. For this reason, the construction industry is highly interested in the development of novel cementitious

binders, preferably based on secondary industrial by-products, with equivalent performance to OPC but with a lower CO₂ footprint [5–7]. One such alternative is supersulfated cement (SSC), which comprises typically a mixture of 70-90 wt.% ground granulated blast furnace slag (GGBFS), 10-20 wt.% calcium sulfate and an alkaline activator (mostly < 5 wt.%), usually OPC or clinker [8]. If the slag has an Al₂O₃ content exceeding 13 wt.%, the hydration could, in **fact**, occur without the addition of an alkaline activator. **However**, most GGBFS is characterized by Al₂O₃ contents lower than 13 wt.% [5], which results in a very slow reaction rate. Therefore, the addition of an alkaline activator (**potentially in combination with adapted curing conditions**) is necessary to accelerate the hydration reaction [8–12]. The use of phosphogypsum (PG) [13–15], a by-product generated in the phosphate industry, as calcium sulfate source further decreases the environmental footprint of SSC. Because PG contains remnants of phosphoric acid (among other impurities such as fluorine), however, its use might result in a higher alkaline-demand for such matrices [16]. PG **might also contain elevated** concentrations of naturally occurring radionuclides [17], which can be problematic when considering its use for building purposes. A previous in-depth investigation into this aspect [18] concluded that a maximum of 10 wt.% PG could be incorporated from a radiological perspective. It should be kept in mind that the radionuclide content of PG streams [19,20], and industrial by-products in general [21,22], can **vary** significantly. **Also, sand and aggregates can either increase or dilute the total radionuclide content of a building material.** Each individual case therefore needs careful evaluation.

The proposed system in this investigation differs from SSCs because it includes 10 wt.% PG as calcium sulfate source, and **completely** excludes the use of OPC by choosing NaOH as alkali activator. Nevertheless, this system might behave in a similar way. Typical hydration products of SSCs are ettringite (AFt, 3CaO·Al₂O₃·3CaSO₄·32H₂O) and monosulfates (AFm, 3CaO·Al₂O₃·CaSO₄·nH₂O where n = 8-14) [23], along with other crystalline or amorphous phases such as e.g. portlandite, aluminum-hydroxide, **calcium-aluminosilicate- hydrate**

(CASH) or calcium-silicate-hydrate (CSH) [24,25]. The NaOH content, however, might significantly influence the hydration product formation and final assemblage.

This study therefore investigates the influence of the NaOH content on the hydration, mineralogy, porosity and compressive strength using in-situ and ex-situ X-ray diffraction (XRD), isothermal calorimetry, thermogravimetric analysis (TGA), Fourier-transformed infrared (FTIR) spectroscopy, nitrogen adsorption/desorption and compressive strength tests.

In contrast to previous studies on alkali-activated binders from 90 wt.% GGBFS and 10 wt.% PG [18,26,27], this study aims to decrease the alkali content in view of increased production safety, and lower production costs and environmental footprint imposed by the production of alkalis [28] (while simultaneously obtaining adequate properties).

2. Materials and methods

2.1 Materials

GGBFS was supplied by a Belgian iron and steel production company. PG was collected from a PG processing plant in Gdansk (Poland), and subsequently milled and homogenized by the International Atomic Energy Agency (IAEA) (reference material IAEA 434) [29].

GGBFS was dried in a laboratory oven at 110 °C, and thereafter milled to a Blaine fineness of 4050 ± 200 cm²/g, measured according to EN 196-6 [30]. The density of GGBFS was 2.9 g/cm³, determined according to ASTM C204 [31] with a Quantachrome Multipycnometer MVP-6DC. The particle size distribution of GGBFS and PG was investigated by laser scattering (Mastersizer Micro Plus, Malvern, Worcestershire, UK) using isopropanol to avoid hydration during the measurement, and is presented in Fig. 1. GGBFS showed a bimodal particle size distribution from 0.1 µm to 103.6 µm and a d_{50} of 10 µm. PG (used as received) presents an unimodal particle size distribution from 0.2 µm to 24 µm and a d_{50} of 7 µm.

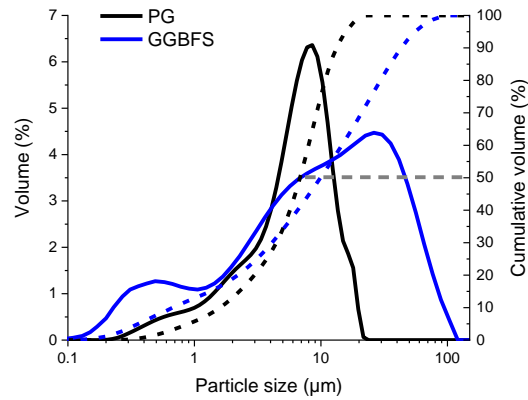


Figure 1: Particle size distribution of GGBFS and PG

The chemical composition of GGBFS was investigated by X-ray fluorescence (XRF) analysis (Philips PW 1830), while the chemical composition of PG was provided by the IAEA. The results are summarized in Table 1.

Table 1: Chemical composition (in wt.%) of GGBFS and PG

Chemical compound	GGBFS	PG
CaO	44.1	35.2
SiO ₂	32.5	0.9
Al ₂ O ₃	10.5	0.2
MgO	8.6	-
SO ₃	1.8	50.3
TiO ₂	0.8	-
K ₂ O	0.5	-
Na ₂ O	0.4	-
Fe ₂ O ₃	0.3	-
P ₂ O ₅	-	1.3
F ⁻	-	1.1
LOI at 950 °C	0.1	11.0

XRD analysis was carried out to investigate the mineralogy of GGBFS and PG. As an internal standard, 10 wt.% ZnO (purity 99.9%, Merck) was added [32,33]. The measurements were performed using a D2 PHASER (Bruker) automated diffractometer with Cu-K α -radiation equipped with a Lynx-eye super speed position sensitive detector, operated at 30 kV and 10 mA in continuous PSD (position sensitive detector) fast mode. The scan range was from 5° to 70° 2 θ , the step width was 0.02° 2 θ , and the counting time was 0.3 s per step. A beam knife slit was positioned 3 mm above the sample, which was prepared using the back loading technique. During acquisition, the sample was rotated at 15 rpm. The diffractograms obtained are shown in Fig. 2 and the peaks from ZnO are indicated with an asterisk.

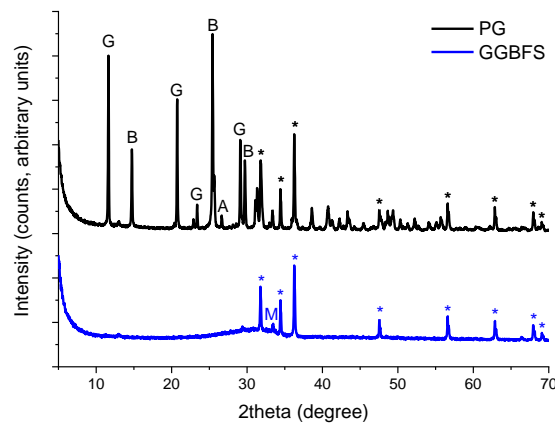


Figure 2: Diffractograms obtained from XRD of GGBFS and PG (merwinite: M, gypsum: G, bassanite: B, anhydrite: A)

Qualitative analysis of the diffractograms was performed with EVA V.3.1 (Bruker AXS) software. For quantitative analysis, MAUD (Material Analysis Using Diffraction) [34] was used based on the Rietveld method [35–37] and the background was fitted by a 15 coefficient polynomial function [38]. From the known initial ZnO content, the crystalline and amorphous contents were recalculated, and the results are summarized in Table 2.

Table 2: Mineralogy (in wt.%) of GGBFS and PG

Phase	GGBFS	PG
-------	-------	----

Merwinite ($\text{Ca}_3\text{MgSi}_2\text{O}_8$)	5.3 ± 0.8	-
Gypsum ($\text{CaSO}_4 \cdot 2\text{H}_2\text{O}$, $\text{C}\bar{\text{S}}\text{H}_2$)	-	33.2 ± 0.9
Bassanite ($\text{CaSO}_4 \cdot 0.5\text{H}_2\text{O}$, $\text{C}\bar{\text{S}}\text{H}_{0.5}$)	-	27.1 ± 0.9
Anhydrite (CaSO_4 , $\text{C}\bar{\text{S}}$)	-	32.1 ± 1.0
Amorphous	94.7 ± 0.8	7.6 ± 2.8

2.2 Sample mixtures

Based on a previous radiological investigation [18], a maximum of 10 wt.% PG can be incorporated in order to comply with the European Union Basic Safety Standards (EU-BSS) for building materials [39]. Therefore, a mixture of 90 wt.% GGBFS and 10 wt.% PG was chosen. The GGBFS and PG were mixed for 2 h in a Turbula T2C mixer for homogenization (referred to as 'binder'). Chemical grade NaOH (purity 99%, Chem-Lab) and distilled water (ASTM type II) were used for the synthesis of the alkali activators, which was done 1 day prior to sample preparation. The $\text{H}_2\text{O}/\text{Na}_2\text{O}$ molar ratios of the alkali activators (taking into account the density of the solutions at 20 °C) were 55.56/0.00 (0 M NaOH), 55.56/0.25 (0.5 M NaOH), 55.56/0.50 (1 M NaOH), 55.56/1.00 (2 M NaOH), 55.00/1.50 (3 M NaOH) and 55.00/2.00 (4 M NaOH). A total of 6 pastes (P1-P6) and 6 mortars (M1-M6) were prepared. The details of the mixtures are summarized in Table 3. Based on previous experimental work [18,26,27], the alkali activator/binder weight ratio (AA/B) was established at 3/5 and was retained for all pastes and mortars for the sake of comparison. For the preparation of the pastes, the alkali activator was manually mixed with the binder for 3 min. Due to the small volumes involved, manual mixing was chosen instead of using a Hobart mixer in order to obtain good homogeneity. For the preparation of the mortars, CEN standard sand (DIN EN 196-1) was used with a sand/binder weight ratio (S/B) of 3/1 according to EN 196-1 [40]. The mixing of the mortars was performed in accordance with EN 196-6 [30]. All pastes and mortars were prepared under laboratory conditions (room temperature 20 ± 2 °C, relative

humidity about 50%). The SO_3 content of the binder amounts to 6 wt.%, which is consistent with the requirements of the European standard for SSCs ($5 \text{ wt.\%} \leq \text{SO}_3 \leq 12 \text{ wt.\%}$) [41].

Table 3: Sample mixtures

Sample*	Binder		Alkali activator	AA/B	S/B
	wt.% GGBFS	wt.% PG	$\text{H}_2\text{O}/\text{Na}_2\text{O}$ (NaOH molarity)		
P1, M1	90	10	55.56/0.00 (0 M)	3/5	0/1, 3/1
P2, M2	90	10	55.56/0.25 (0.5 M)	3/5	0/1, 3/1
P3, M3	90	10	55.56/0.50 (1 M)	3/5	0/1, 3/1
P4, M4	90	10	55.56/1.00 (2 M)	3/5	0/1, 3/1
P5, M5	90	10	55.00/1.50 (3 M)	3/5	0/1, 3/1
P6, M6	90	10	55.00/2.00 (4 M)	3/5	0/1, 3/1

*P1-P6 and M1-M6 refer to pastes and mortars, respectively.

2.3 Sample dimensions and curing regimes

For in-situ XRD and isothermal calorimetry on fresh pastes, the measurements were executed immediately after the mixing procedure. For XRD, TGA, FTIR and nitrogen adsorption/desorption, fresh pastes were cast in polystyrene cubic molds with dimensions 25 mm × 25 mm × 25 mm and covered with plastic film to avoid water evaporation and carbonation. After 24 h, the pastes were demolded and further cured in plastic bags under laboratory conditions (temperature $20 \pm 2 \text{ }^\circ\text{C}$, relative humidity about 50%). For XRD, the curing times were 3, 7, 14 and 28 days. For TGA, FTIR and nitrogen adsorption/desorption, the curing time amounted to 28 days. There was no need to stop the hydration (with e.g. isopropanol) as all measurements were scheduled exactly in time. For compressive strength testing, fresh mortars were cast in polymer coated steel molds with dimensions 40 mm × 40 mm × 160 mm and vibrated for 60 s at a frequency of 1 Hz [30]. A plastic film was placed over the opening surface of the molds to prevent water evaporation and carbonation. After 24 h, the mortars were demolded and further cured in plastic vessels for 28 days under

laboratory conditions (temperature 20 ± 2 °C, relative humidity about 50%). M1 was demolded after 14 days because it did not gain enough strength during the first 24 h, whereafter the same curing regime was applied as for the other mortars.

2.4 In-situ XRD and isothermal calorimetry

For in-situ XRD measurements, the same D2 PHASER (Bruker) diffractometer was used as for the XRD analysis of the materials. After the mixing procedure, the fresh pastes were poured into the sample holder (25 mm diameter and 1 mm depth), and the surface was smoothed. No internal standard was added because of the potential influence on the hydration product formation. The sample holder was sealed with Kapton film to prevent water evaporation and carbonation. A total of 110 diffractograms were recorded in continuous PSD fast mode between 6° and 55° 2θ at time intervals of 13 min, with a step width of 0.02° 2θ and a counting time of 0.3 s per step. The X-ray tube was operated at 30 kV and 10 mA. A beam knife slit was positioned 1 mm above the sample and the temperature inside the diffractometer case was kept constant at 20 °C during acquisition. The diffractograms were qualitatively evaluated with EVA V.3.1 (Bruker AXS) software.

A TAM-Air Isothermal Calorimeter (TA Instruments) was used for heat flow calorimetry under isothermal conditions (20.0 ± 0.1 °C) during the first 6 days of hydration. After the mixing procedure, the fresh pastes were poured into glass ampoules, which were inserted in the calorimeter. P1 was additionally monitored for 28 days.

2.5 XRD

After their curing period (i.e., 3, 7, 14 and 28 days), the hardened pastes were manually milled in a porcelain mortar. P1 could not be measured after 3 and 7 days because it did not gain enough strength. As an internal standard, 10 wt.% ZnO (purity 99.9%, Merck) was

added [32,33]. The measurements were performed using the same diffractometer, settings and procedure as for the XRD analysis of the materials. A beam knife slit was positioned 1 mm above the sample. Qualitative and quantitative analysis were performed in the same way as for the materials.

2.6 TGA, FTIR and nitrogen adsorption/desorption

After their curing period (i.e., 28 days), the hardened pastes were investigated. Prior to TGA and FTIR, the pastes were manually milled in a porcelain mortar. TGA (Q55, TA Instruments) was carried out on a sample weight of 20 mg under nitrogen atmosphere from room temperature to 995 °C at a heating rate of 10 °C/min. For FTIR, a Vertex 70 spectrometer (Bruker) with an ATR diamond crystal (Pike) was used. Spectra were acquired in wavenumber ranges from 4000 cm⁻¹ to 600 cm⁻¹ at a resolution of 4 cm⁻¹ and with 32 scans per measurement, using a DTGS detector. Nitrogen adsorption/desorption tests were carried out using a TRISTAR 3000 Micromeritics device at -196.2 °C. Prior to degassing, the pastes were dried in a laboratory oven at 40 °C for 2-3 days until a constant weight was achieved. Thereafter, they were degassed using the vacuum degas method with a Schlenk line at 20 °C for 72 h at a pressure/vacuum of 100 Pa. The specific surface area was obtained from the adsorption data by the BET (Brunauer, Emmett and Teller) method [42] over the P/P_0 range of 0.05-0.30 (where P is the partial vapor pressure of the adsorbate gas in equilibrium and P_0 is the saturated pressure of the adsorbate gas at -196.2 °C). From the desorption data, the mesopore size distribution and the cumulative mesopore volume were found using the BJH (Barrett, Joyner and Halenda) method [43]. The micropore volume and micropore surface area were obtained from the adsorption data using the T-plot analysis method [44].

2.7 Compressive strength testing

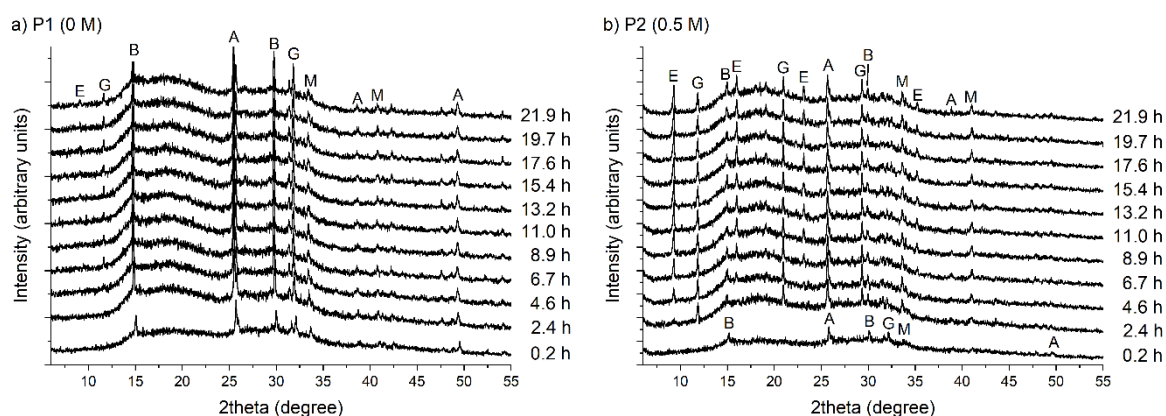
After their curing period (i.e., 28 days), the hardened mortars were tested for their compressive strength. An Instron 5985 machine equipped with a 250 kN load cell was employed for testing 5 specimens of each formulation.

3. Results and discussion

3.1 In-situ XRD and isothermal calorimetry

In Fig. 3, a selection of the recorded in-situ XRD diffractograms are plotted (at regular time steps of 130 min) for P1-P6. Quantitative analysis of those data is not feasible as no internal standard was added. The following phases were recognized: merwinite, gypsum, bassanite, anhydrite, ettringite, CASH [45–47], portlandite, a monosulfate phase, and thenardite. The monosulfate phase constitutes $\text{NaCa}_4\text{Al}_2\text{O}_6(\text{SO}_4)_{1.5} \cdot 15\text{H}_2\text{O}$ (PDF 44-0272 in the PDF1999-database). The hump in the diffractograms from approximately 12° to 25° 2θ is mainly caused by the presence of Kapton film, while the remaining water in the sample contributes to a lesser extent to the broader hump from approximately 12° to 45° 2θ . From Fig. 3a, it is clear that the mineralogy of the paste remains quite similar during the first 24 h upon mixing the binder with a 0 M NaOH solution. The peaks in the diffractograms mainly originate from merwinite, gypsum, bassanite and anhydrite from the binder. When increasing the molarity of the NaOH solution from 0.5 M to 4 M (Fig. 3b to Fig. 3f), the dissolution of the binder and the formation of hydration products, simultaneously or in sequence, is recognizable in the diffractograms. For example, the formation of ettringite at around 9° 2θ is clearly distinguishable in Fig. 3b and Fig. 3c and the intensity of this peak grew slightly over time. The higher the molarity, the faster the peaks from the binder disappear and peaks from the hydration products appear, suggesting a faster setting time. However, even at the highest molarities of 3 M and 4 M, merwinite is still present at 21.9 h, which may be due to an initial fast coverage of the binder by the hydration products, hindering proper dissolution of the binder. Gypsum and bassanite appear to dissolve more easily compared to anhydrite, which is still present in P3 after 21.9 h. A similar effect is described in [48–50]. From a molarity of 1

M and higher, the formation of CASH is deduced from the hump at around $29^\circ 2\theta$ [46,47]. Another peak typical for the CASH phase appears gradually for P6 at around $7^\circ 2\theta$ [51]. At a molarity of 1 M, portlandite is initially formed and remains present in the paste until approximately 3-4 h after mixing. At a molarity of 2 M, initially formed portlandite remains present in the paste until approximately 4-6 h after mixing. At a molarity of 3 M and 4 M, portlandite is recognized in all diffractograms. The formation of portlandite increases the pH and promotes further slag dissolution [25]. Therefore, from a molarity of 1 M and higher, the system behaves as a hybrid one consisting of a cascade of amplifying reactions. As further discussed in section 3.3, P3-P6 showed the lowest porosity. Ettringite is formed in P1-P4. At a molarity of 2 M, ettringite and a rather crystalline monosulfate phase coexist, while at molarities of 3 M and 4 M only the monosulfate phase is present in the sample, and ettringite is absent. Thenardite (Na_2SO_4) appears in P6 approximately 10-11 h after mixing. The formation of thenardite, which is a soluble salt, is undesirable from the leaching point of view. For P6, all intensities drop away after 16 h, which is likely to be the consequence of sample swelling or shrinkage, obscuring proper diffraction at the sample surface. Volume expansion due to the (partial) dissolution of the monosulfate phase might be a possible explanation [52], which then induces thenardite formation.



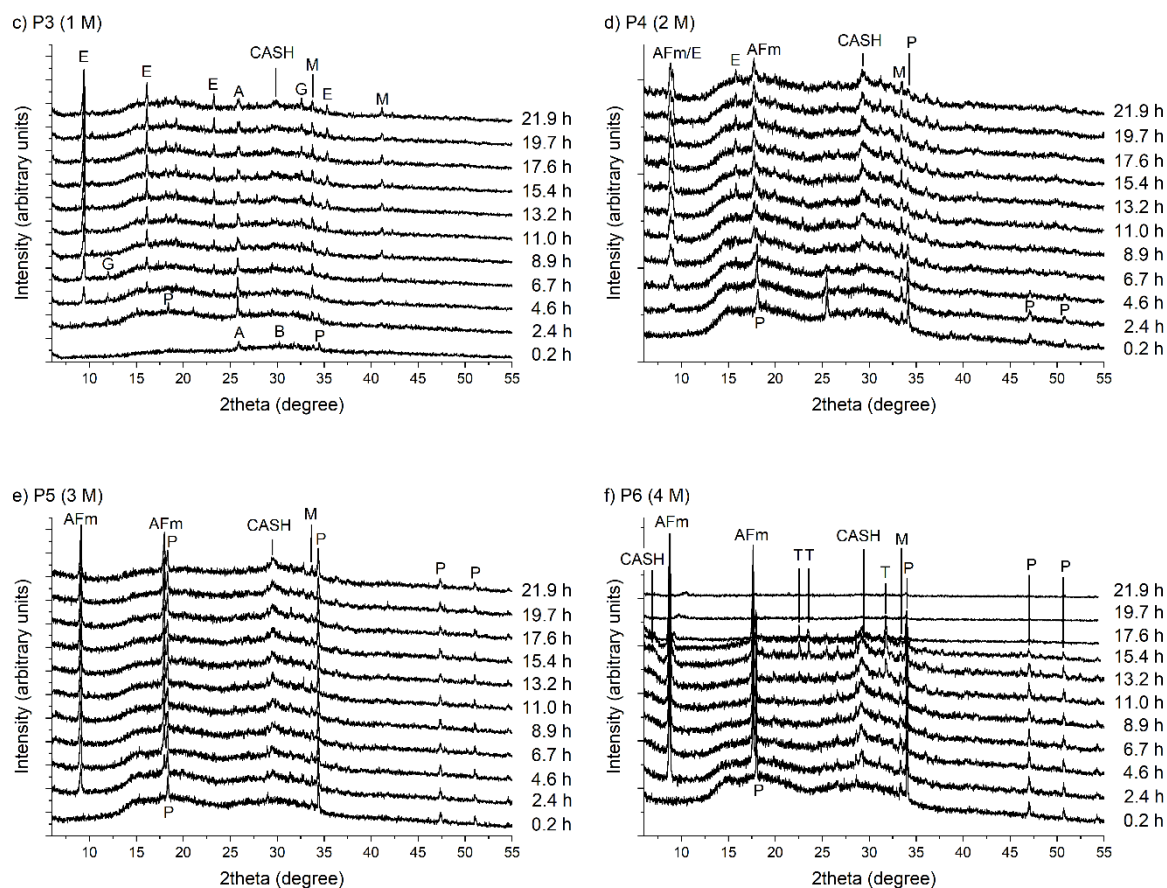


Figure 3: Diffractograms obtained from in-situ XRD for a) P1, b) P2, c) P3, d) P4, e) P5 and f) P6 (merwinite: M, gypsum: G, bassanite: B, anhydrite: A, ettringite: E, calcium-

aluminosilicate-hydrate: CASH, portlandite: P, a monosulfate phase: AFm, and thenardite: T)

The heat release and cumulative heat during the first 6 days of hardening are shown in Fig. 4a (and during the first 24 h in Fig. 4b and Fig. 4c). For all samples, an initial wetting and dissolution peak is observed after inserting the paste into the calorimeter. For P1, which was prepared with a 0 M NaOH solution, no exothermic reactions took place during the first 6 days. The initial exothermic peak between 0 h and 2 h for P2, P3 and P4 (the combination of wetting and dissolution) is followed by an induction period of approximately 3 h, whereafter a second exothermic peak from 5 h to 60 h is presumably caused by the formation of hydration products (which is consistent with in-situ XRD where the ettringite peak became clearly visible after 4.6 h). For P5 and P6, no induction period is observed between the first and second exothermic peak, indicating that immediately after dissolution a critical concentration

271 was reached to initiate the hydration product formation (consistent with in-situ XRD, where
272 e.g. portlandite was already recognized in the first diffractogram). The heat release curve of
273 P6 is significantly different from the other curves because of its major heat release during the
274 first 10 h, followed later by a sharp increase in heat release after 40 h. A potential cause
275 might be the initial coverage of a portion of the binder due to a fast initial hydration product
276 formation (e.g. the fast initial formation of the monosulfate phase during the first 10 h), which
277 gets further hydrated after 40 h. The same phenomenon has been reported in [25,53,54].
278 The cumulative heat of P2, P3 and P4 is comparable, reaching around 80 J/g after 6 days.
279 Comparable values are reported in the literature [55]. The cumulative heat for P5 and P6 is
280 25% (100 J/g) and 50% (124 J/g) higher at that time, respectively. Fig. 4a shows that
281 hydration is an ongoing process that continues even after 6 days. The calorimetric monitoring
282 of P1 was prolonged to 28 days and the curves are presented in Fig. 4d. After the initial
283 wetting and dissolution peak, a very long induction period is observed until approximately
284 160 h, followed by a second exothermic peak that reaches a maximum at 200 h. From these
285 data, it is assumed that the setting of P1 starts only after 7 days. After 28 days, the
286 cumulative heat of P1 reached 116 J/g. To be in accordance with the European standard for
287 SSCs, the cumulative heat at 7 days should not exceed 220 J/g [41]. SSCs have the
288 advantage of generating a much lower heat during hydration compared to OPC [56]. The
289 combined effect of OPC's low thermal conductivity and its high heat during hydration might
290 induce cracking [57].

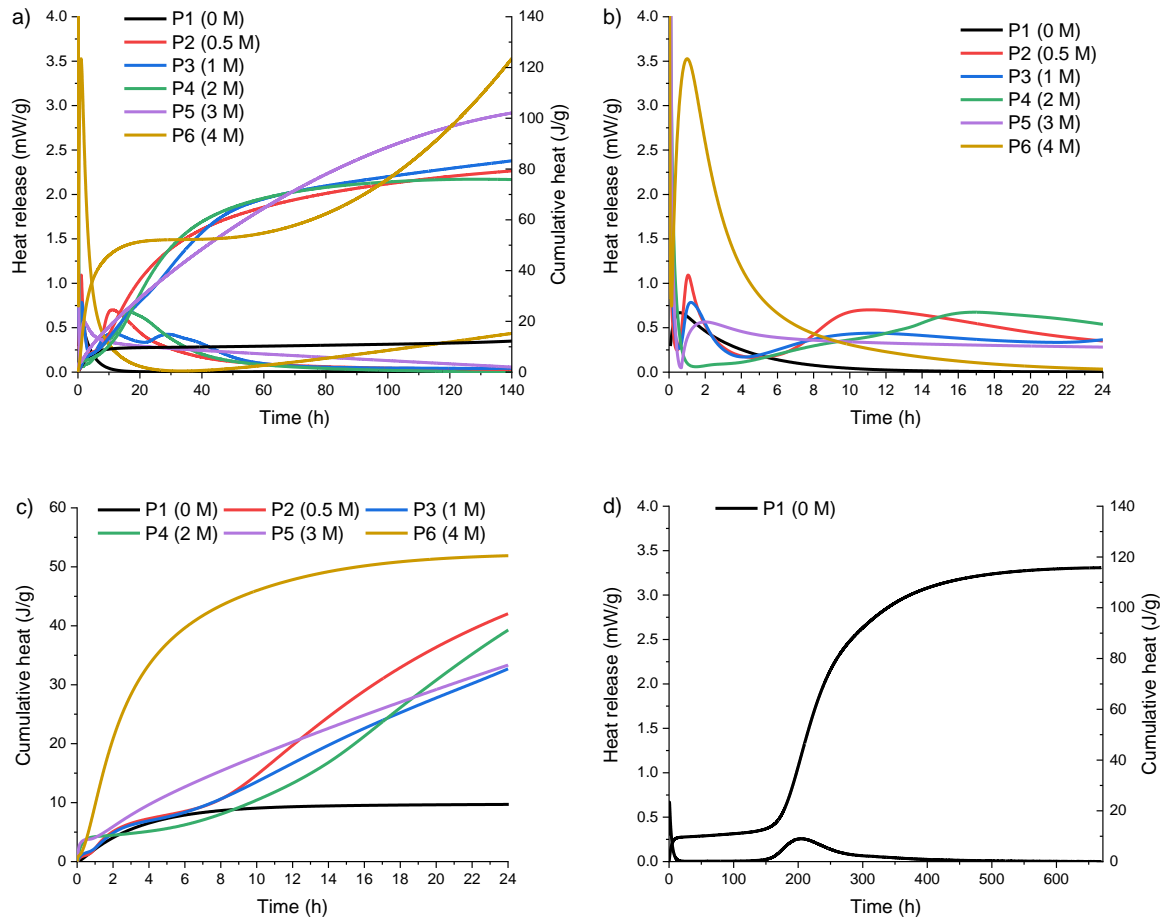
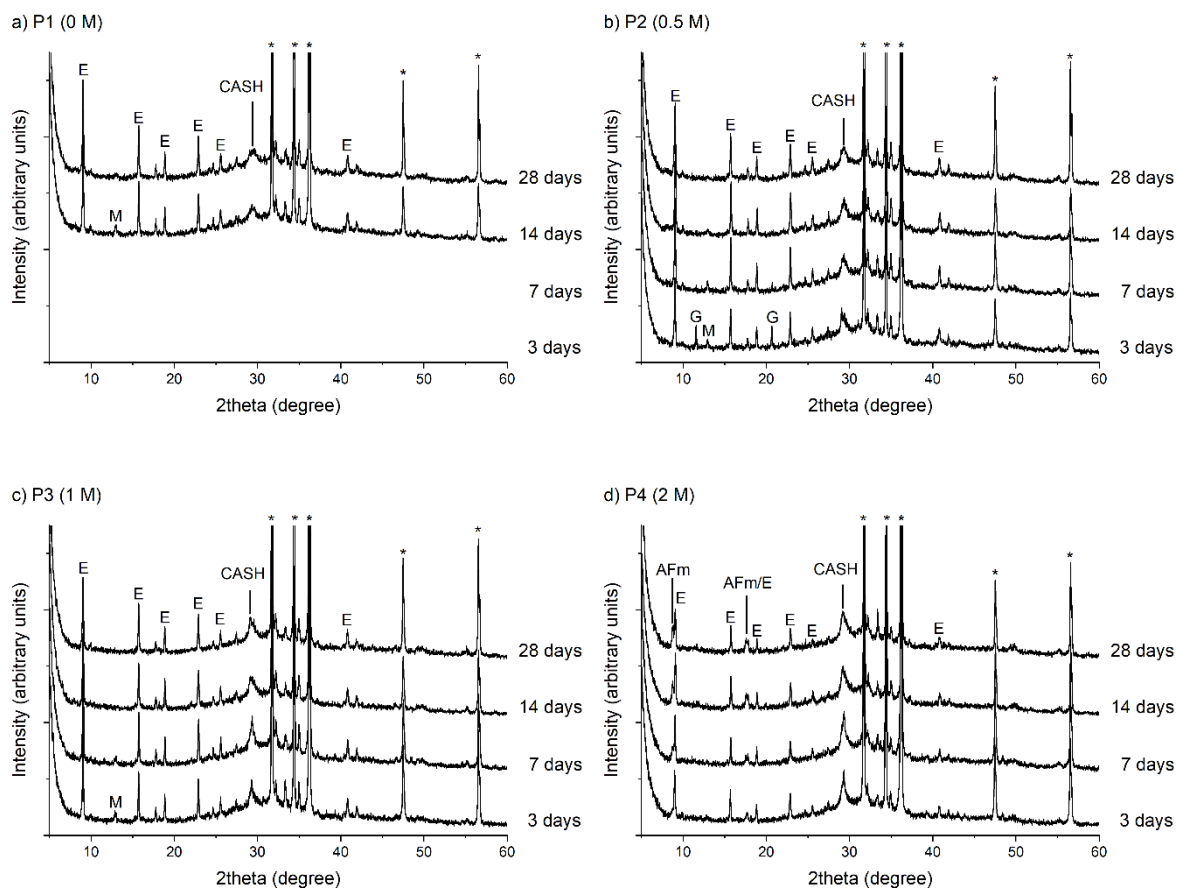


Figure 4: a) Heat release and cumulative heat during 6 days for P1-P6, b) heat release during 24 h for P1-P6, c) cumulative heat during 24 h for P1-P6, and d) heat release and cumulative heat during 28 days for P1

3.2 XRD

XRD analysis was performed after curing periods of 3, 7, 14 and 28 days. The diffractograms are plotted from 5° to 60° 2θ and are presented in Fig. 5. P1 did not gain enough strength after 3 and 7 days and could therefore only be measured after 14 and 28 days of curing. The peaks of ZnO are indicated with an asterisk. Merwinite and gypsum originate from the undissolved GGBFS and PG particles, respectively. It has to be noted here that thenardite and calcite (not indicated in Fig. 5) are considered to be side-products. The main hydration products identified were ettringite, CASH [45–47], a monosulfate phase [47,58], and

portlandite. As with in-situ XRD (section 3.1), the monosulfate phase constitutes $\text{NaCa}_4\text{Al}_2\text{O}_6(\text{SO}_4)_{1.5} \cdot 15\text{H}_2\text{O}$. Other minor hydration products (not indicated in Fig. 5) found were cuspidine and $\text{Mg}_2\text{P}_2\text{O}_7$. An amorphous aluminum-hydroxide phase is also expected to be present (further confirmed by TGA in section 3.3 for P4-P6), yet not recognizable by XRD [48]. The presence of a CSH phase could not be identified due to its highly amorphous nature, yet it is visible for P1-P4 in TGA (section 3.3). Anhydrite and bassanite were not recognized, while merwinite and gypsum peaks gradually disappear upon extended curing times. From a molarity of 2 M and higher, neither merwinite nor gypsum peaks were observed. The peaks originating from the hydration products grew slightly over time. Upon increasing the molarity of the alkali activator, CASH development is promoted, as well as the monosulfate phase. As with in-situ XRD, ettringite and monosulfate coexist in P4, while ettringite is absent in P5 and P6.



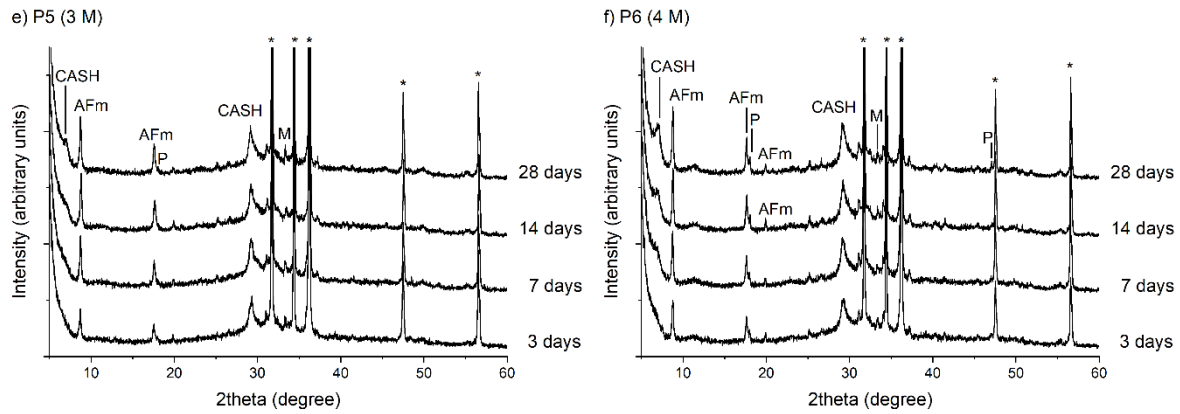


Figure 5: Diffractograms obtained from XRD after 3, 7, 14 and 28 days of curing for a) P1, b) P2, c) P3, d) P4, e) P5 and d) P6 (merwinite: M, gypsum: G, ettringite: E, calcium-aluminosilicate-hydrate: CASH, portlandite: P, and a monosulfate phase: AFm)

Fig. 6 compares the diffractograms obtained after 28 days of curing for the different samples. From Fig. 6, the shift from ettringite (P1, P2, P3, P4) to the monosulfate phase (i.e., $\text{NaCa}_4\text{Al}_2\text{O}_6(\text{SO}_4)_{1.5} \cdot 15\text{H}_2\text{O}$) (P4, P5, P6) is clearly distinguishable at around 8 to $9^\circ 2\theta$ and at around 17° to $18^\circ 2\theta$ [58]. In most cases monosulfate phases are amorphous and difficult to quantify using XRD [59–61], although in this system this phase appears to be rather crystalline. Portlandite (near 18° and $47^\circ 2\theta$) is observed for P5 and P6. For all samples, the intensity of the CASH peak at around $29^\circ 2\theta$ [46,47] (and at around $7^\circ 2\theta$ [51] for P5 and P6) gradually increases when the molarity of the alkali activator is increased, while the full width at half maximum (FWHM) gradually decreases. This suggests that the presence and crystallinity of the CASH phase is increasing, when the molarity of the alkali activator is increased.

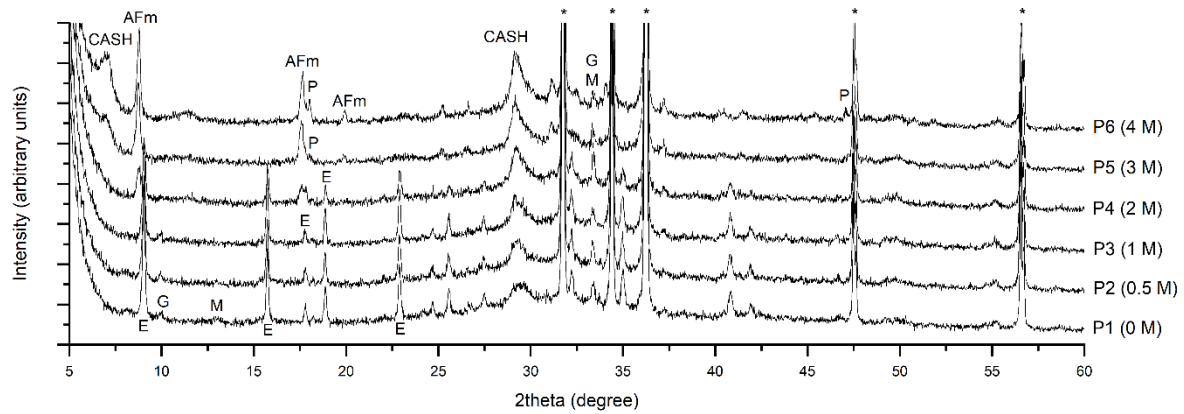


Figure 6: Diffractograms obtained from XRD after 28 days of curing (merwinite: M, gypsum: G, ettringite: E, calcium-aluminosilicate-hydrate: CASH, portlandite: P, and a monosulfate phase: AFm)

Fig. 7 gives the quantitative XRD (QXRD) analysis. As mentioned, due to insufficient strength development, P1 was only measured after 14 and 28 days of curing. It should be noted that CASH, CSH and aluminum-hydroxide are ascribed to the amorphous part. Overall, the phase assemblage continues to develop after 3 days of curing. Anhydrite and bassanite are not present, while gypsum and merwinite from the binder gradually disappear with extended curing times, and their dissolution is enhanced by an increased molarity of the alkali activator. Approximately 8 wt.% of ettringite was present for P1-P3, while from a molarity of 2 M and above ettringite gradually disappeared and the monosulfate phase showed up. Cuspidine and $\text{Mg}_2\text{P}_2\text{O}_7$ are more favored at higher molarities, their content gradually increased upon increasing the curing time for all samples. Portlandite peaks were clearly distinguishable in the in-situ XRD diffractograms for P3-P6 (section 3.1). For P3 and P4, this phase gradually disappears upon extended curing periods and performs as an intermediate (hydration) product. For P5 and P6, portlandite was recognized during the first 22 h of hydration, whereafter its content slightly increased from 3 days up to 28 days of curing. Thenardite and calcite are, as already mentioned, considered to be side-products. Thenardite was found for all samples, while the calcite content was highest at molarities of 3 M and 4 M.

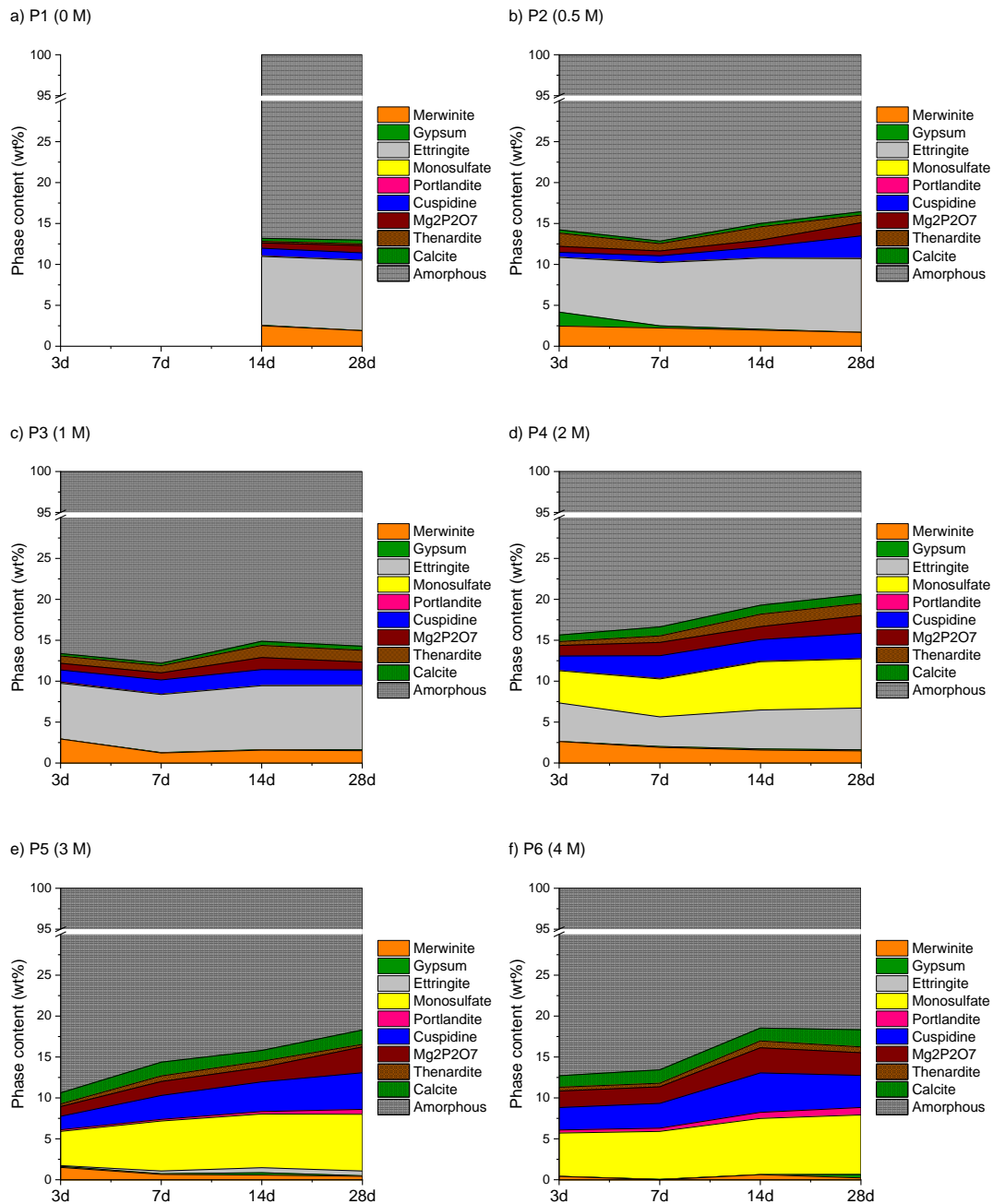


Figure 7: QXRD after 3, 7, 14 and 28 days of curing for a) P1, b) P2, c) P3, d) P4, e) P5 and d) P6

Fig. 8 provides the quantitative analysis of the diffractograms after 28 days of curing in function of the NaOH molarities of the alkali activators. Ettringite converts to the monosulfate phase from a molarity of 2 M and above. The stability of this monosulfate phase should be investigated further. The cuspidine and $Mg_2P_2O_5$ content gradually increases when the molarity is increased, which is likely to be related to the enhanced GGBFS dissolution

(inversely proportional to the decreasing merwinite content upon increasing the molarity). Gypsum in P5 and P6 might be secondary gypsum [25], which can exert adverse effects on the strength if it is formed after final setting. The potential occurrence of delayed ettringite formation (DEF) [62] at later ages for P4-P6 will be dependent on the Ca^{2+} , Al^{3+} and SO_4^{2-} balance in the pore solution and its pH, and should be elucidated.

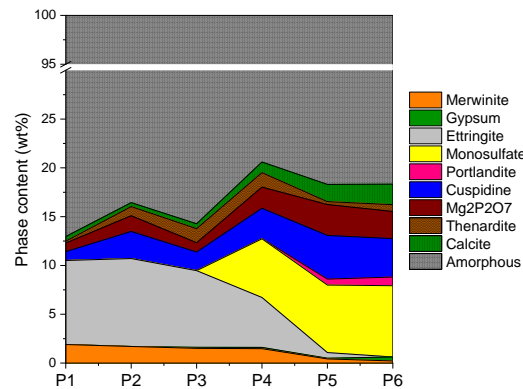


Figure 8: QXRD after 28 days of curing

3.3 TGA, FTIR and nitrogen adsorption/desorption

The thermogravimetric (TG) and derivative thermogravimetric (DTG) curves are shown in Fig. 9. The mass loss under 90 °C is caused by the loss of bound water (P5-P6) and the decomposition of ettringite [63] (P1-P4) (see Fig. 9b). Monosulfate is recognized for P4-P6 (consistent with XRD and QXRD) from 110-170 °C [48]. Contrary to XRD analysis, amorphous aluminum-hydroxide is detectable due to its water loss at around 270 °C [64], and was only present from a molarity of 2 M and higher. The TG/DTG results revealed the presence of hydrogarnet ($3\text{CaO} \cdot \text{Al}_2\text{O}_3 \cdot 6\text{H}_2\text{O}$) for P4-P6, which decomposes at around 325 °C [65]. This phase might be formed due to the higher heat release during curing for those samples, which is in agreement with [60,66–69] where it was observed that hydrogarnet formed under hydrothermal curing conditions (e.g. in [67] hydrogarnet was formed at 90 °C, in [68] formation of hydrogarnet is predicted at temperatures above 50 °C). Hydrogarnet is

thermodynamically stable in the temperature range from 20 to 250 °C [70,71]. Remnants of portlandite were highest for P6, which agrees with QXRD. The condensation of structural hydroxyl groups from the CSH phase is recognized at 610-630 °C [72] for P1-P4. As this phase was not found in the XRD diffractograms of P1-P4, this CSH phase is expected to be highly amorphous. The CSH phase is not observed for P5-P6 in the TG/DTG curves, which is also consistent with XRD in section 3.2 where it was found that a semi-amorphous CASH showed up when the molarity of the alkali activator was increased, which also caused its crystallinity to increase. A similar observation is presented in [25], where a low alkaline content increased CSH formation and higher alkalinities increased its crystallinity. The weight loss at 750 °C corresponds to the decomposition of CaCO_3 to CaO and CO_2 [73]. Calcite was also confirmed by QXRD after 28 days of curing, where the highest content was found for P6.

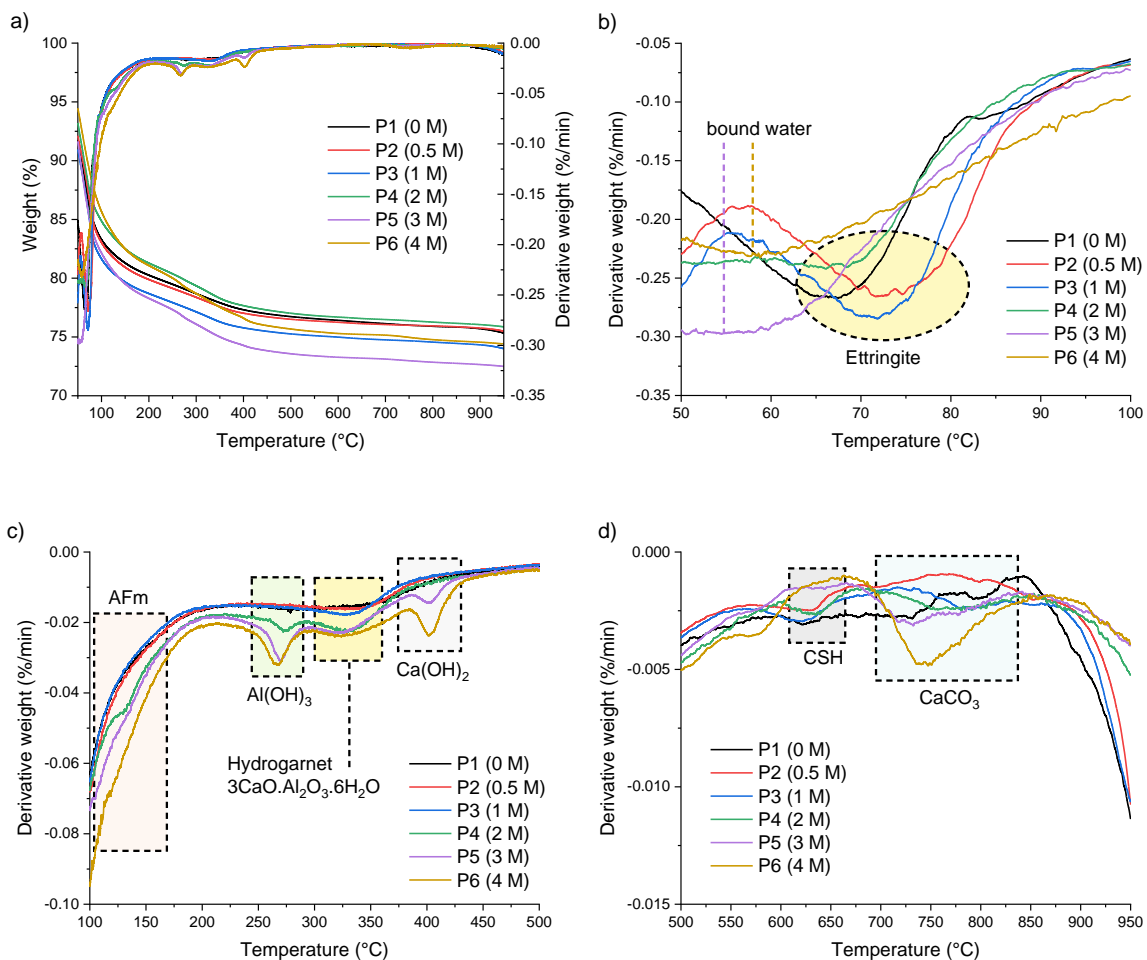


Figure 9: a) TG and DTG curves after 28 days of curing, b) DTG curves from 50 to 100 °C, c) DTG curves from 100 to 500 °C and d) DTG curves from 500 to 950 °C

The FTIR spectra are shown in Fig. 10. The bands located between 3750 cm^{-1} and 3000 cm^{-1} and near 1600 cm^{-1} are assigned to O-H vibrations [74,75]. The bands at around 960 cm^{-1} and 850 cm^{-1} are related to the Al-O-H bond [76], while the S-O bond stretching occurs at 1100 cm^{-1} (asymmetrical ν_3 vibrations) and at 660 cm^{-1} (asymmetrical ν_4 vibrations) [77,78]. The FTIR spectra provide evidence of the gradual disappearance of ettringite when the molarity of the alkali activator is increased, which is in agreement with XRD and TGA. It should be kept in mind, however, that other phases such as the monosulfate phase, aluminum-hydroxide or gypsum may contribute to those bands as well, which is difficult to distinguish in FTIR spectra. The C-O bonding is evident in the band near 1400 cm^{-1} [79,80] and molarities of 2 M and higher gave rise to an increased carbonation compared to lower molarities, which is also seen in the QXRD and TGA data. The stretching vibrations of the Si-O-T units (where T stands for Al or Si) are clearly distinguishable for P5 and P6 at 940 cm^{-1} (typical for Q^2 units) [81–84] and at 800 cm^{-1} (typical for Q^1 units) [84,85], while both bands are absent for P1-P4. None of the samples contained Q^3 Si-O-T units, which are normally recognized from a band around 1200 cm^{-1} [84]. The intensity of the Si-O-T bands was highest for P5, while the intensity for P6 was lower. As confirmed by XRD, those bands originate from a CASH phase (as these bands are not observed for P1-P4). The location and breadth of the Si-O-T bands for P5 and P6 is comparable, indicating similar amorphousness and Ca/Si and Al/Si ratios [86].

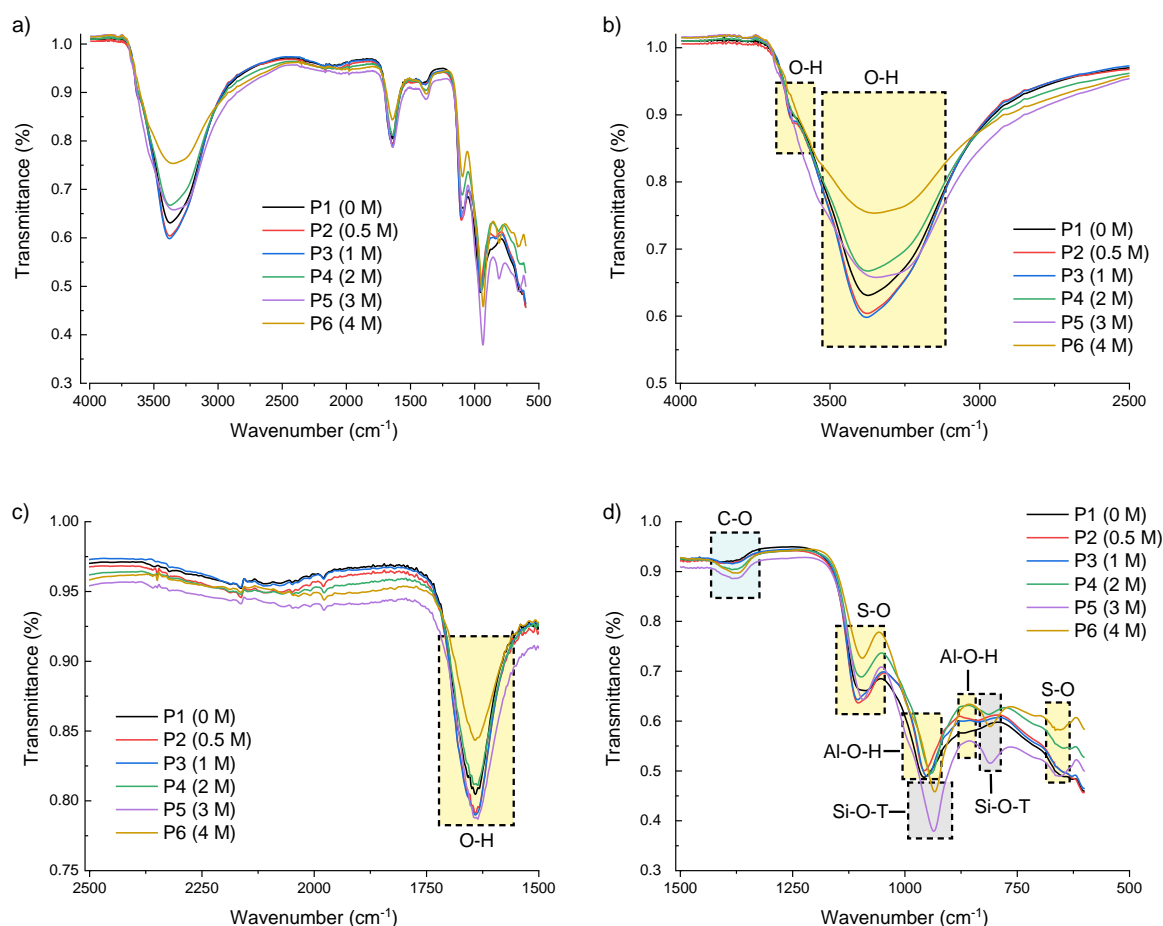


Figure 10: a) FTIR curves after 28 days of curing, b) FTIR curves from 4000 to 2500 cm^{-1} , c) FTIR curves from 2500 to 1500 cm^{-1} and d) FTIR curves from 1500 to 500 cm^{-1}

The results from nitrogen adsorption/desorption tests are presented in Fig. 11. The isotherms in Fig. 11a are characterized by a type IIb shape [87] with an H5 (P1, P2 and P3) or an H3 (P4, P5 and P6) hysteresis loop [88], indicating that the meso- and macropores in those samples are predominant in addition to fewer slit-shaped micropores. The H5 hysteresis loop is typical for structures containing both open and partially blocked mesopores, while an H3 hysteresis loop indicates plate-like particles (as in certain clays) [88]. The plateau at high relative pressure suggests that all pores were filled [89]. An increase in the molarity of the alkali activator resulted generally in a decreased maximum amount of nitrogen adsorbed at the maximum relative pressure (a non-linear relation is observed) and a decreased hysteresis loop surface. Fig. 11b presents the pore surface area obtained using the BET and T-plot methods. The surface area of the pores generally decreases when the molarity of the

alkali activator is increased, although a small increase is noted when moving from a 1 M to a 2 M solution. The decrease in pore surface area is expected to be caused by a higher dissolution rate of the precursors and consequently a denser hydration product matrix. OPC typically has a pore surface area (obtained with nitrogen adsorption/desorption and the BET method) of around 50 m²/g [90], which is 2-5 times higher than the pore surface area of the pastes in this investigation. The mesopore size distribution, obtained using the BJH method (cylindrical pores are hypothesized for the calculation), is plotted in Fig. 11c. As the pore shape remains unknown, however, those results are indicative (nevertheless comparative for this series of samples) [89]. It should also be noted that the valid pore size range is from 2-30 nm, due to the upper P/P_0 limit of around 0.97 [91,92]. P1 shows a bimodal profile, with a sharp peak from 3-4 nm and a much broader one from 4-25 nm. P2 and P3 are also characterized by a bimodal distribution although the peaks occur at lower pore diameters with a maximum at 3 nm and 4 nm. P4, P5 and P6 show a unimodal distribution with a maximum at 4 nm. The pore volume is presented in Fig. 11d, where generally a decrease is observed when the molarity of the alkali activator is increased, which is likely to be due to an increasing precursor dissolution grade when moving from P1 to P6 and the effect of carbonation.

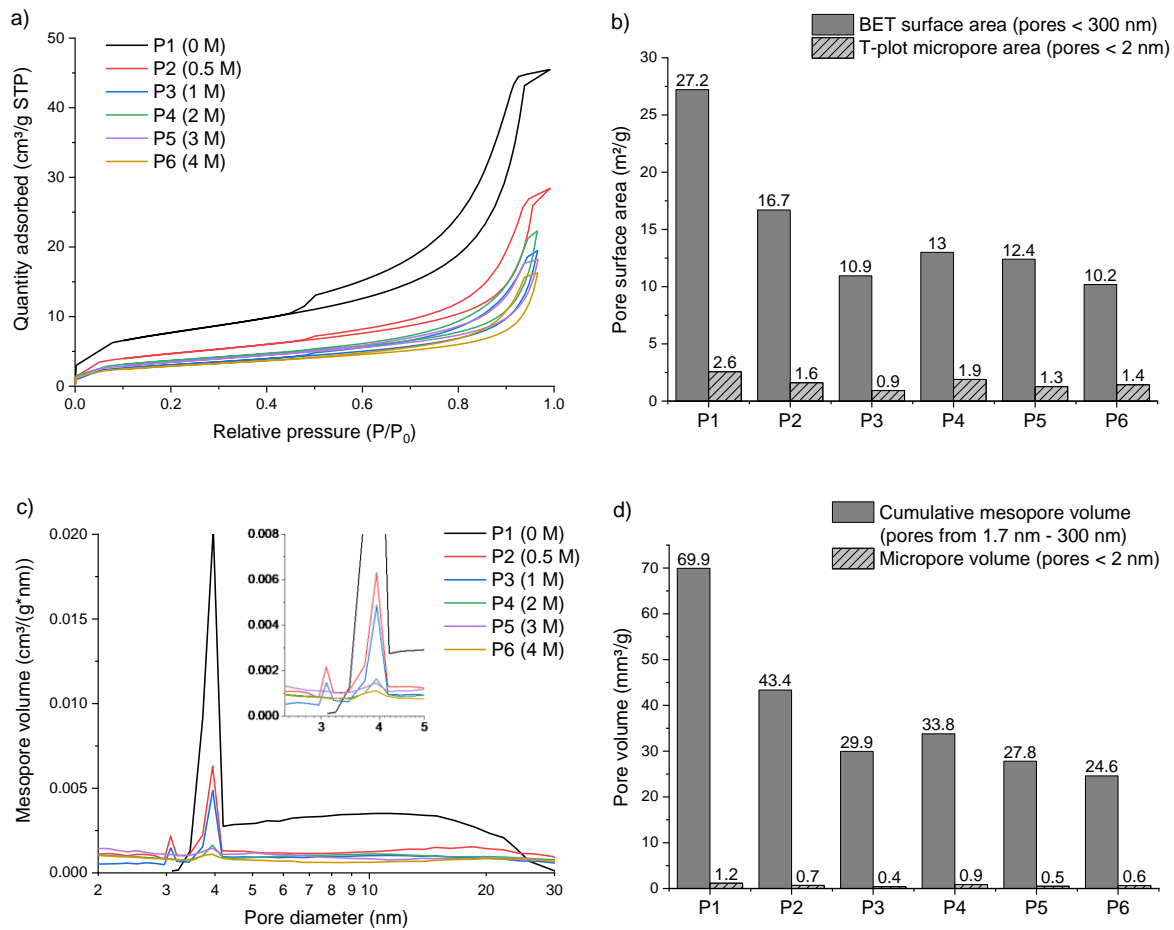


Figure 11: Nitrogen adsorption/desorption data after 28 days of curing: a) adsorption/desorption isotherms, b) pore surface area, c) mesopore size distribution and d) pore volume

3.4 Compressive strength

The compressive strength (1σ error) of the mortars after 28 days of curing is shown in Fig. 12. Although P1 was characterized by a very long setting time of over 7 days, M1 reaches the highest compressive strength (41.8 ± 1.2 MPa) after 28 days of curing. The strength of M2-M5 is in the same order of magnitude (16.5 ± 1.2 MPa, 14.0 ± 0.7 MPa, 16.2 ± 0.1 MPa and 12.6 ± 0.7 MPa, respectively), while the strength of M6 is slightly higher (23.4 ± 1.5 MPa). A high heat release might confirm the hydration of a significant amount of reaction products. The cumulative heat of P1 was, however, not significantly higher compared to P5

and P6. After 28 days, the cumulative heat of P1 was 116 J/g. The cumulative heat of P5 and P6 reached 100 J/g and 124 J/g, respectively, after 6 days. A denser matrix often leads to a higher strength, but P1 was characterized by the highest porosity. A high ettringite content can result in an increased strength. However, the ettringite content of P1 and P2 was comparable (8.6 wt.% and 9.0 wt.%, respectively), while the compressive strength of M2 was less than half of M1. The high compressive strength of M1 might be due to its highest amorphous content (87.0 wt.%) and/or lowest cuspidine and $\text{Mg}_2\text{P}_2\text{O}_7$ content (0.9 wt.% and 0.9 wt.%, respectively). Also, the amorphous CSH content was highest for P1 in TGA. The European standard for SSCs [41] includes minimum characteristic values for cement but not for mortars. The minimum compressive strength at 28 days should be 32.5 MPa for pastes [41], though it should be kept in mind that mortar strength is often actually lower than pure paste strength [93].

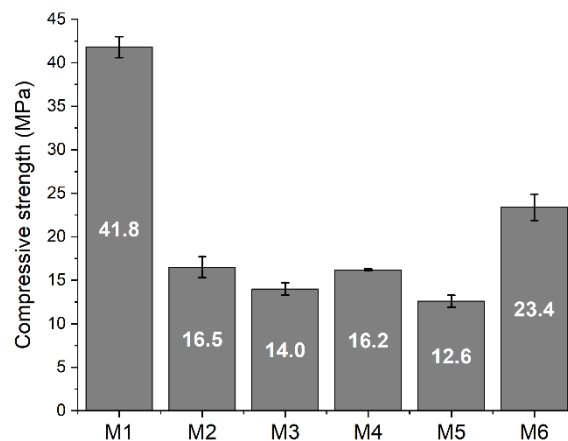


Figure 12: Compressive strength of mortars after 28 days of curing

4. Conclusions

This study investigated the effect of the NaOH content on alkali/sulfate-activated binders from 90 wt.% GGBFS and 10 wt.% PG. Alkali activators were prepared with a NaOH molarity ranging from 0 M to 4 M. The hydration, mineralogy, porosity and compressive strength of the produced pastes and mortars were investigated. **These are the main conclusions:**

- A molarity of 0 M gave rise to the highest porosity and highest strength, although the setting occurred only after 7 days.
- At molarities of 1 M and higher, portlandite appeared during the first few hours of hardening and acted as a catalyst that promoted further slag dissolution.
- The molarity of the alkali activator significantly influenced the phase assemblage, which developed continuously during the first 28 days. At lower molarities (from 0 M to 1 M), an amorphous CSH phase was present, while molarities of 2 M and higher favored CASH development, together with cuspidine and $\text{Mg}_2\text{P}_2\text{O}_7$.
- From a molarity of 2 M and higher, ettringite disappeared and was replaced by a monosulfate phase (i.e., $\text{NaCa}_4\text{Al}_2\text{O}_6(\text{SO}_4)_{1.5} \cdot 15\text{H}_2\text{O}$) and amorphous aluminum-hydroxide. Their content gradually increased as the curing time was increased for all samples.
- The formation of thenardite, which is a salt, is undesirable from the leaching point of view.
- Carbonation was enhanced when the molarity of the alkali activator was increased. From the environmental point of view, however, carbonation should not necessarily be viewed as unwanted, as long as it has no negative influence on the properties and durability of the material, due to its ability to capture atmospheric CO_2 .

Further investigation of the mineralogy, porosity and strength over extended curing times (e.g. over 1-3 years) is advised in order to define appropriate applications.

Declarations of interest: none

Acknowledgements

This work was supported by the Fund for Scientific Research Flanders (FWO). The authors would like to thank the networking support of the COST Action TU1301, www.norm4building.org. Marcin Selent (University of Oulu, Finland) and Kristof Van Hecke

(University of Ghent, Belgium) are gratefully acknowledged for their valuable feedback with respect to XRD.

References

- [1] E. Benhelal, G. Zahedi, E. Shamsaei, A. Bahadori, Global strategies and potentials to curb CO₂ emissions in cement industry, *J. Clean. Prod.* 51 (2013) 142–161. doi:10.1016/j.jclepro.2012.10.049.
- [2] H.G. van Oss, A.C. Padovani, Cement manufacture and the environment - Part II: Environmental challenges and opportunities, *J. Ind. Ecol.* 7 (2003) 93–126. doi:10.1162/108819802320971650.
- [3] E.M. Gartner, D.E. MacPhee, A physico-chemical basis for novel cementitious binders, *Cem. Concr. Res.* 41 (2011) 736–749. doi:10.1016/j.cemconres.2011.03.006.
- [4] D.J.M. Flower, J.G. Sanjayan, Green house gas emissions due to concrete manufacture, *Int. J. Life Cycle Assess.* 12 (2007) 282–288. doi:10.1065/lca2007.05.327.
- [5] M.C.G. Juenger, F. Winnefeld, J.L. Provis, J.H. Ideker, Advances in alternative cementitious binders, *Cem. Concr. Res.* 41 (2011) 1232–1243. doi:10.1016/j.cemconres.2010.11.012.
- [6] C. Shi, A.F. Jiménez, A. Palomo, New cements for the 21st century: The pursuit of an alternative to Portland cement, *Cem. Concr. Res.* 41 (2011) 750–763. doi:10.1016/j.cemconres.2011.03.016.
- [7] E. Gartner, Industrially interesting approaches to “low-CO₂” cements, *Cem. Concr. Res.* 34 (2004) 1489–1498. doi:10.1016/j.cemconres.2004.01.021.
- [8] H.F.W. Taylor, *Cement chemistry*, 2nd ed., Thomas Telford Publishing, London, 1997.
- [9] I.G. Richardson, C.R. Wilding, M.J. Dickson, The hydration of blastfurnace slag cements, *Adv. Cem. Res.* 2 (1989) 147–157. doi:10.1680/adcr.1989.2.8.147.
- [10] C. Shi, X. Wu, M. Tang, Research on alkali-activated cementitious systems in China: a review, *Adv. Cem. Res.* 5 (1993) 1–7. doi:10.1680/adcr.1993.5.17.1.
- [11] S. Samad, A. Shah, M.C. Limbachiya, Strength development characteristics of concrete produced with blended cement using ground granulated blast furnace slag (GGBS) under various curing conditions, *Sadhana - Acad. Proc. Eng. Sci.* 42 (2017) 1203–1213. doi:10.1007/s12046-017-0667-z.
- [12] S. Aydin, B. Baradan, Mechanical and microstructural properties of heat cured alkali-activated slag mortars, *Mater. Des.* 35 (2012) 374–383. doi:10.1016/j.matdes.2011.10.005.

- 546 [13] E. Saadaoui, N. Ghazel, C. Ben Romdhane, N. Massoudi, Phosphogypsum: potential
547 uses and problems – a review, *Int. J. Environ. Stud.* 74 (2017) 558–567.
548 doi:10.1080/00207233.2017.1330582.
- 549 [14] P.M. Rutherford, M.J. Dudas, R.A. Samek, Environmental impacts of phosphogypsum,
550 *Sci. Total Environ.* 149 (1994) 1–38. doi:10.1016/0048-9697(94)90002-7.
- 551 [15] H. Tayibi, M. Choura, F.A. López, F.J. Alguacil, A. López-Delgado, Environmental
552 impact and management of phosphogypsum, *J. Environ. Manage.* 90 (2009) 2377–
553 2386. doi:10.1016/j.jenvman.2009.03.007.
- 554 [16] L. Reijnders, Cleaner phosphogypsum, coal combustion ashes and waste incineration
555 ashes for application in building materials: A review, *Build. Environ.* 42 (2007) 1036–
556 1042. doi:10.1016/j.buildenv.2005.09.016.
- 557 [17] K. Kovler, M. Somin, Producing environment-conscious building materials from
558 contaminated phosphogypsum, in: N. Kashino, Y. Ohama (Eds.), *Int. RILEM Symp.*
559 *Environ. Mater. Syst. Sustain. Dev.*, RILEM Publications S.A.R.L., Koriyama, Japan,
560 2004: pp. 245–253. doi:10.1617/2912143640.029.
- 561 [18] K. Gijbels, R. Ion Iacobescu, Y. Pontikes, N. Vandevenne, S. Schreurs, W. Schroeyers,
562 Radon immobilization potential of alkali-activated materials containing ground
563 granulated blast furnace slag and phosphogypsum, *Constr. Build. Mater.* 184 (2018)
564 68–75. doi:10.1016/j.conbuildmat.2018.06.162.
- 565 [19] P.M. Rutherford, M.J. Dudas, J.M. Arocena, Radioactivity and elemental composition
566 of phosphogypsum produced from three phosphate rock sources, *Waste Manag. Res.*
567 (1995). doi:10.1177/0734242X9501300502.
- 568 [20] K. Gijbels, H. Nguyen, P. Kinnunen, W. Schroeyers, Y. Pontikes, S. Schreurs, M.
569 Illikainen, Feasibility of incorporating phosphogypsum in ettringite-based binder from
570 ladle slag, *J. Clean. Prod.* 237 (2019) 117793. doi:10.1016/j.jclepro.2019.117793.
- 571 [21] C. Nuccetelli, Y. Pontikes, F. Leonardi, R. Trevisi, New perspectives and issues arising
572 from the introduction of (NORM) residues in building materials: A critical assessment
573 on the radiological behaviour, *Constr. Build. Mater.* 82 (2015) 323–331.
574 doi:10.1016/j.conbuildmat.2015.01.069.
- 575 [22] Z. Sas, N. Vandevenne, R. Doherty, R. Vinai, J. Kwasny, M. Russell, W. Sha, M.
576 Soutsos, W. Schroeyers, Radiological evaluation of industrial residues for construction
577 purposes correlated with their chemical properties, *Sci. Total Environ.* 658 (2019) 141–
578 151. doi:10.1016/j.scitotenv.2018.12.043.
- 579 [23] H. Pöllmann, Synthesis, properties and solid solution of ternary lamellar calcium
580 aluminate hydroxi salts (AFm-phases) containing SO₄²⁻, CO₃²⁻ and OH⁻, *J. Mineral.*
581 *Geochemistry.* 182 (2006) 173–181. doi:10.1127/0077-7757/2006/0042.
- 582 [24] D.K. Dutta, P.C. Borthakur, Activation of low lime high alumina granulated blast

- 583 furnace slag by anhydrite, *Cem. Concr. Res.* 20 (1990) 711–722. doi:10.1016/0008-
584 8846(90)90005-I.
- 585 [25] S. Rubert, C.A. Luz, M.V.F. Varela, J.I.P. Filho, R.D. Hooton, Hydration mechanisms
586 of supersulfated cement: The role of alkali activator and calcium sulfate content, *J.*
587 *Therm. Anal. Calorim.* 134 (2018) 971–980. doi:10.1007/s10973-018-7243-6.
- 588 [26] K. Gijbels, S. Landsberger, P. Samyn, R. Ion Iacobescu, Y. Pontikes, S. Schreurs, W.
589 Schroyers, Radiological and non-radiological leaching assessment of alkali-activated
590 materials containing ground granulated blast furnace slag and phosphogypsum, *Sci.*
591 *Total Environ.* 660 (2019) 1098–1107. doi:10.1016/j.scitotenv.2019.01.089.
- 592 [27] K. Gijbels, R.I. Iacobescu, Y. Pontikes, S. Schreurs, W. Schroyers, Alkali-activated
593 binders based on ground granulated blast furnace slag and phosphogypsum, *Constr.*
594 *Build. Mater.* 215 (2019) 371–380. doi:10.1016/j.conbuildmat.2019.04.194.
- 595 [28] B.C. McLellan, R.P. Williams, J. Lay, A. Van Riessen, G.D. Corder, Costs and carbon
596 emissions for geopolymer pastes in comparison to ordinary portland cement, *J. Clean.*
597 *Prod.* 19 (2011) 1080–1090. doi:10.1016/j.jclepro.2011.02.010.
- 598 [29] A. Shakhashiro, U. Sansone, H. Wershofen, A. Bollhöfer, C.K. Kim, C.S. Kim, G. Kis-
599 Benedek, M. Korun, M. Moune, S.H. Lee, S. Tarjan, M.S. Al-Masri, The new IAEA
600 reference material: IAEA-434 technologically enhanced naturally occurring radioactive
601 materials (TENORM) in phosphogypsum, *Appl. Radiat. Isot.* 69 (2011) 231–236.
602 doi:10.1016/j.apradiso.2010.09.002.
- 603 [30] European Committee for Standardization, EN 196-6. Methods of testing cement - Part
604 6: Determination of fineness, (2010).
- 605 [31] ASTM International, ASTM C204-17. Standard test methods for fineness of hydraulic
606 cement by air-permeability apparatus, (2017).
- 607 [32] D. Jansen, C. Stabler, F. Goetz-Neunhoeffler, S. Dittrich, J. Neubauer, Does Ordinary
608 Portland Cement contain amorphous phase? A quantitative study using an external
609 standard method, *Powder Diffr.* 26 (2011) 31–38. doi:10.1154/1.3549186.
- 610 [33] I.C. Madsen, N.V.Y. Scarlett, A. Kern, Description and survey of methodologies for
611 the determination of amorphous content via X-ray powder diffraction, *Zeitschrift Für*
612 *Krist.* 226 (2011) 944–955. doi:10.1524/zkri.2011.1437.
- 613 [34] L. Lutterotti, S. Matthies, H.R. Wenk, MAUD (Material Analysis Using Diffraction): a
614 user friendly java program for Rietveld texture analysis and more, in: Jerzy A. Szipunar
615 (Ed.), *Proc. Twelfth Int. Conf. Textures Mater. / ICOTOM-12*, National Research
616 Press, Montreal, 1999: p. 1599.
- 617 [35] H.M. Rietveld, A profile refinement method for nuclear and magnetic structures, *J.*
618 *Appl. Crystallogr.* 2 (1969) 65–71. doi:10.1107/S0021889869006558.
- 619 [36] R.W. Cheary, A.A. Coelho, A fundamental parameter approach to X-ray line-profile

- fitting, *J. Appl. Crystallogr.* 25 (1992) 109–121. doi:10.1107/S0021889891010804.
- [37] D.L. Bish, S.A. Howard, Quantitative phase analysis using the Rietveld method, *J. Appl. Crystallogr.* 21 (1988) 86–91. doi:10.1107/S0021889887009415.
- [38] R. Snellings, L. Machiels, G. Mertens, J. Elsen, Rietveld refinement strategy for quantitative phase analysis of partially amorphous zeolitized tuffaceous rocks, *Geol. Belgica*. 13 (2010) 183–196. doi:10.1590/S1806-83242009000100002.
- [39] Council of the European Union, Council directive 2013/59/EURATOM, European Basic Safety Standards (BSS) for Protection against Ionising Radiation, *Off. J. Eur. Union*. L 13/1 (2014).
- [40] European Committee for Standardization, EN 196-1. Methods of testing cement - Part 1: Determination of strength, (2016).
- [41] European Committee for Standardization, EN 15743. Supersulfated cement: Composition, specification and conformity criteria, (2010).
- [42] S. Brunauer, P.H. Emmett, E. Teller, Adsorption of gases in multimolecular layers, *J. Am. Chem. Soc.* 60 (1938) 309–319. doi:10.1021/ja01269a023.
- [43] E.P. Barrett, L.G. Joyner, P.P. Halenda, The determination of pore volume and area distributions in porous substances. I. Computations from nitrogen isotherms, *J. Am. Ceram. Soc.* 73 (1951) 373–380. doi:10.1021/ja01145a126.
- [44] B.C. Lippens, J.H. de Boer, Studies on pore systems in catalysts: V. The t method, *J. Catal.* 4 (1965) 319–323. doi:10.1016/0021-9517(65)90307-6.
- [45] H.F.W. Taylor, Nanostructure of C-S-H: Current status, *Adv. Cem. Based Mater.* 1 (1993) 38–46. doi:10.1016/1065-7355(93)90006-A.
- [46] G. Renaudin, J. Russias, F. Leroux, C. Cau-dit-Coumes, F. Frizon, Structural characterization of C-S-H and C-A-S-H samples - Part II: Local environment investigated by spectroscopic analyses, *J. Solid State Chem.* 182 (2009) 3320–3329. doi:10.1016/j.jssc.2009.09.024.
- [47] E. Kapeluszna, Ł. Kotwica, A. Różycka, Ł. Gołek, Incorporation of Al in C-A-S-H gels with various Ca/Si and Al/Si ratio: Microstructural and structural characteristics with DTA/TG, XRD, FTIR and TEM analysis, *Constr. Build. Mater.* 155 (2017) 643–653. doi:10.1016/j.conbuildmat.2017.08.091.
- [48] F. Winnefeld, B. Lothenbach, Hydration of calcium sulfoaluminate cements - Experimental findings and thermodynamic modelling, *Cem. Concr. Res.* 40 (2010) 1239–1247. doi:10.1016/j.cemconres.2009.08.014.
- [49] M.Z. Lan, B.F. Xiang, J.F. Wang, X.D. Zhao, X.Y. Wang, Effect of anhydrite on the early hydration performance of rapid setting and hardening belite sulfoaluminate cement, *Mater. Sci. Forum.* 898 (2017) 1990–1995.

- doi:10.4028/www.scientific.net/MSF.898.1990.
- [50] M. García-maté, A.G. De la Torre, L. León-reina, E.R. Losilla, M.A.G. Aranda, I. Santacruz, Effect of calcium sulfate source on the hydration of calcium sulfoaluminate eco-cement, *Cem. Concr. Compos.* 55 (2015) 53–61.
doi:10.1016/j.cemconcomp.2014.08.003.
- [51] Y. Jeong, C.W. Hargis, S.C. Chun, J. Moon, The effect of water and gypsum content on strätlingite formation in calcium sulfoaluminate-belite cement pastes, *Constr. Build. Mater.* 166 (2018) 712–722. doi:10.1016/j.conbuildmat.2018.01.153.
- [52] R. Khoshnazar, J.J. Beaudoin, R. Alizadeh, L. Raki, Volume stability of calcium sulfoaluminate phases, *J. Am. Ceram. Soc.* 95 (2012) 3979–3984.
doi:10.1111/jace.12040.
- [53] T. Matschei, F. Bellmann, J. Stark, Hydration behaviour of sulphate-activated slag cements, *Adv. Cem. Res.* (2005) 167–178. doi:10.1680/adcr.2005.17.4.167.
- [54] K.J. Mun, W.K. Hyoun, C.W. Lee, S.Y. So, Y.S. Soh, Basic properties of non-sintering cement using phosphogypsum and waste lime as activator, *Constr. Build. Mater.* 21 (2007) 1342–1350. doi:10.1016/j.conbuildmat.2005.12.022.
- [55] S. Liu, L. Wang, Y. Gao, B. Yu, W. Tang, Influence of fineness on hydration kinetics of supersulfated cement, *Thermochim. Acta.* 605 (2015) 37–42.
doi:10.1016/j.tca.2015.02.013.
- [56] D. Jansen, C. Naber, D. Ectors, Z. Lu, X.M. Kong, F. Goetz-Neunhoffer, J. Neubauer, The early hydration of OPC investigated by in-situ XRD, heat flow calorimetry, pore water analysis and ¹H NMR: Learning about adsorbed ions from a complete mass balance approach, *Cem. Concr. Res.* 109 (2018) 230–242.
doi:10.1016/j.cemconres.2018.04.017.
- [57] B. Lothenbach, K. Scrivener, R.D. Hooton, Supplementary cementitious materials, *Cem. Concr. Res.* 41 (2011) 1244–1256. doi:10.1016/j.cemconres.2010.12.001.
- [58] N. Ukrainczyk, T. Matusinovic, S. Kurajica, B. Zimmermann, J. Sipusic, Dehydration of a layered double hydroxide - C₂AH₈, *Thermochim. Acta.* 464 (2007) 7–15.
doi:10.1016/j.tca.2007.07.022.
- [59] D. Gastaldi, G. Paul, L. Marchese, S. Irico, E. Boccaleri, S. Mutke, L. Buzzi, F. Canonico, Hydration products in sulfoaluminate cements: Evaluation of amorphous phases by XRD/solid-state NMR, *Cem. Concr. Res.* 90 (2016) 162–173.
doi:10.1016/j.cemconres.2016.05.014.
- [60] G. Le Saout, E. Lécuyer, A. Rivereau, H. Zanni, Chemical structure of cement aged at normal and elevated temperatures and pressures, *Cem. Concr. Res.* 36 (2004) 71–78.
doi:10.1016/j.cemconres.2004.09.018.
- [61] T. Matschei, B. Lothenbach, F.P. Glasser, The AFm phase in Portland cement, *Cem.*

- 693 Concr. Res. 37 (2007) 118–130. doi:10.1016/j.cemconres.2006.10.010.
- 694 [62] S. Diamond, Delayed ettringite formation - Processes and problems, Cem. Concr.
695 Compos. 18 (1996) 205–215. doi:10.1016/0958-9465(96)00017-0.
- 696 [63] T. Grounds, H.G. Midgley, D.V. Nowell, The use of thermal methods to estimate the
697 state of hydration of calciumtrisulphoaluminate hydrate $3\text{CaO} \cdot \text{Al}_2\text{O}_3 \cdot 3\text{CaSO}_4 \cdot n\text{H}_2\text{O}$,
698 Thermochim. Acta. 85 (1985) 215–218. doi:10.1016/0040-6031(85)85567-2.
- 699 [64] S.W. Tang, H.G. Zhu, Z.J. Li, E. Chen, H.Y. Shao, Hydration stage identification and
700 phase transformation of calcium sulfoaluminate cement at early age, Constr. Build.
701 Mater. 75 (2015) 11–18. doi:10.1016/j.conbuildmat.2014.11.006.
- 702 [65] Q. Zhou, F.P. Glasser, Thermal stability and decomposition mechanisms of ettringite at
703 $<120^\circ\text{C}$, Cem. Concr. Res. 31 (2001) 1333–1339. doi:10.1016/S0008-8846(01)00558-
704 0.
- 705 [66] B.Z. Dilnesa, B. Lothenbach, G. Renaudin, A. Wichser, D. Kulik, Synthesis and
706 characterization of hydrogarnet $\text{Ca}_3(\text{Al}_x\text{Fe}_{1-x})_2(\text{SiO}_4)_y(\text{OH})_{4(3-y)}$, Cem. Concr. Res.
707 59 (2014) 96–111. doi:10.1016/j.cemconres.2014.02.001.
- 708 [67] Y. Jeong, C.W. Hargis, H. Kang, S.C. Chun, J. Moon, The effect of elevated curing
709 temperatures on high ye’elite calcium sulfoaluminate cement mortars, Materials
710 (Basel). 12 (2019) 10–12. doi:10.3390/ma12071072.
- 711 [68] B. Lothenbach, T. Matschei, G. Möschner, F.P. Glasser, Thermodynamic modelling of
712 the effect of temperature on the hydration and porosity of Portland cement, Cem.
713 Concr. Res. 38 (2008) 1–18. doi:10.1016/j.cemconres.2007.08.017.
- 714 [69] N. Neuville, E. Lécotier, G. Aouad, A. Rivereau, D. Damidot, Effect of curing
715 conditions on oilwell cement paste behaviour during leaching: Experimental and
716 modelling approaches, Comptes Rendus Chim. 12 (2009) 511–520.
717 doi:10.1016/j.crci.2008.06.006.
- 718 [70] T. Matschei, B. Lothenbach, F.P. Glasser, Thermodynamic properties of Portland
719 cement hydrates in the system $\text{CaO}-\text{Al}_2\text{O}_3-\text{SiO}_2-\text{CaSO}_4-\text{CaCO}_3-\text{H}_2\text{O}$, Cem. Concr.
720 Res. 37 (2007) 1379–1410. doi:10.1016/j.cemconres.2007.06.002.
- 721 [71] R.B. Peppler, L.S. Wells, The system of lime, alumina, and water from 50°C to 250°C , J. Res. Natl. Bur. Stand. (1934). 52 (1954) 75–92. doi:10.6028/jres.052.013.
- 723 [72] S. Medvešček, R. Gabrovšek, V. Kaučič, A. Meden, Hydration products in water
724 suspension of Portland cement containing carbonates of various solubility, Acta Chim.
725 Slov. 53 (2006) 172–179.
- 726 [73] N.R. Short, P. Purnell, C.L. Page, Preliminary investigations into the supercritical
727 carbonation of cement pastes, J. Mater. Sci. 36 (2001) 35–41.
728 doi:10.1023/A:1004870204162.

- 729 [74] P. Yu, R.J. Kirkpatrick, B. Poe, P.F. McMillan, C. Xiandong, Structure of calcium
730 silicate hydrate (C-S-H): Near-, mid-, and far-infrared spectroscopy, *J. Am. Ceram.*
731 *Soc.* 82 (1999) 742–748. doi:10.1111/j.1151-2916.1999.tb01826.x.
- 732 [75] R.B. Perkins, C.D. Palmer, Solubility of ettringite ($\text{Ca}_6[\text{Al}(\text{OH})_6]_2(\text{SO}_4)_3 \cdot 26\text{H}_2\text{O}$) at
733 5–75°C, *Geochim. Cosmochim. Acta.* 63 (1999) 1969–1980. doi:10.1016/S0016-
734 7037(99)00078-2.
- 735 [76] D. Guimarães, V. de A. Oliveira, V.A. Leão, Kinetic and thermal decomposition of
736 ettringite synthesized from aqueous solutions, *J. Therm. Anal. Calorim.* 124 (2016)
737 1679–1689. doi:10.1007/s10973-016-5259-3.
- 738 [77] E. Scholtzová, L. Kucková, J. Kožíšek, D. Tunega, Structural and spectroscopic
739 characterization of ettringite mineral -combined DFT and experimental study, *J. Mol.*
740 *Struct.* 1100 (2015) 215–224. doi:10.1016/j.molstruc.2015.06.075.
- 741 [78] H. Bensalah, M.F. Bekheet, S. Alami Younssi, M. Ouammou, A. Gurlo, Hydrothermal
742 synthesis of nanocrystalline hydroxyapatite from phosphogypsum waste, *J. Environ.*
743 *Chem. Eng.* 6 (2018) 1347–1352. doi:10.1016/j.jece.2018.01.052.
- 744 [79] M. Yousuf, A. Mollah, T.R. Hess, Y.-N. Tsai, D.L. Cocke, An FTIR and XPS
745 investigations of the effects of carbonation on the solidification/stabilization of cement
746 based systems-Portland type V with zinc, *Cem. Concr. Res.* 23 (1993) 773–784.
747 doi:10.1016/0008-8846(93)90031-4.
- 748 [80] S.A. Bernal, J.L. Provis, V. Rose, R. Mejia De Gutierrez, Evolution of binder structure
749 in sodium silicate-activated slag-metakaolin blends, *Cem. Concr. Compos.* 33 (2011)
750 46–54. doi:10.1016/j.cemconcomp.2010.09.004.
- 751 [81] I. García-Lodeiro, A. Fernández-Jiménez, M.T. Blanco, A. Palomo, FTIR study of the
752 sol-gel synthesis of cementitious gels: C-S-H and N-A-S-H, *J. Sol-Gel Sci. Technol.* 45
753 (2008) 63–72. doi:10.1007/s10971-007-1643-6.
- 754 [82] S.A. Bernal, R. Mejía De Gutiérrez, A.L. Pedraza, J.L. Provis, E.D. Rodriguez, S.
755 Delvasto, Effect of binder content on the performance of alkali-activated slag
756 concretes, *Cem. Concr. Res.* 41 (2011) 1–8. doi:10.1016/j.cemconres.2010.08.017.
- 757 [83] I. García Lodeiro, D.E. Macphee, A. Palomo, A. Fernández-Jiménez, Effect of alkalis
758 on fresh C-S-H gels. FTIR analysis, *Cem. Concr. Res.* 39 (2009) 147–153.
759 doi:10.1016/j.cemconres.2009.01.003.
- 760 [84] N.Y. Mostafa, E.A. Kishar, S.A. Abo-El-Enein, FTIR study and cation exchange
761 capacity of Fe^{3+} - and Mg^{2+} -substituted calcium silicate hydrates, *J. Alloys Compd.*
762 473 (2009) 538–542. doi:10.1016/j.jallcom.2008.06.029.
- 763 [85] F. Gervais, A. Blin, D. Massiot, J.P. Coutures, M.H. Chopinet, F. Naudin, Infrared
764 reflectivity spectroscopy of silicate glasses, *J. Non. Cryst. Solids.* 89 (1987) 384–401.
765 doi:10.1016/S0022-3093(87)80280-6.

- [86] D. Ravikumar, N. Neithalath, Effects of activator characteristics on the reaction product formation in slag binders activated using alkali silicate powder and NaOH, *Cem. Concr. Compos.* 34 (2012) 809–818. doi:10.1016/j.cemconcomp.2012.03.006.
- [87] J. Rouquerol, F. Rouquerol, K.S.W. Sing, P. Llewellyn, G. Maurin, Adsorption by powders and porous solids: Principles, methodology and applications, 2nd ed., Academic Press, Waltham, 2014.
- [88] M. Thommes, K. Kaneko, A. V. Neimark, J.P. Olivier, F. Rodriguez-Reinoso, J. Rouquerol, K.S.W. Sing, Physisorption of gases, with special reference to the evaluation of surface area and pore size distribution (IUPAC Technical Report), *Pure Appl. Chem.* 87 (2015) 1051–1069. doi:10.1515/pac-2014-1117.
- [89] K. Scrivener, R. Snellings, B. Lothenbach, eds., A practical guide to microstructural analysis of cementitious materials, 1st ed., CRC Press, 2018. doi:10.1201/b19074.
- [90] W. Kurdowski, Cement and concrete chemistry, Springer, Krakow, Poland, 2014. doi:10.1007/978-94-007-7945-7.
- [91] K.K. Aligizaki, Pore structure of cement-based materials: Testing, interpretation and requirements, 1st ed., CRC Press, New York, 2005.
- [92] J. Kaufmann, R. Loser, A. Leemann, Analysis of cement-bonded materials by multi-cycle mercury intrusion and nitrogen sorption, *J. Colloid Interface Sci.* 336 (2009) 730–737. doi:10.1016/j.jcis.2009.05.029.
- [93] X. Chen, S. Wu, J. Zhou, Experimental and modeling study of dynamic mechanical properties of cement paste, mortar and concrete, *Constr. Build. Mater.* 47 (2013) 419–430. doi:10.1016/j.conbuildmat.2013.05.063.